Fluorescent protein lifetimes report increased local densities and phases of nuclear condensates during embryonic stem cell differentiation

Khalil Joron[1], Juliane Oliveira Viegas[2], Liam Haas-Neill[3], Sariel Bier[1,2], Paz Drori[1], Shani Dvir[1], Patrick Siang Lin Lim[2], Sarah Rauscher[3], Eran Meshorer[2,4], Eitan Lerner[1,5]

[1] Department of Biological Chemistry, The Alexander Silberman Institute of Life Sciences, Faculty of Mathematics & Science, The Edmond J. Safra Campus, The Hebrew University of Jerusalem, Jerusalem 9190401, Israel.

[2] Department of Genetics, The Alexander Silberman Institute of Life Sciences, The Hebrew University of Jerusalem, Edmond J. Safra Campus, Givat Ram, Jerusalem, 91904, Israel.

[3] Department of Chemical and Physical Sciences, University of Toronto Mississauga, Mississauga, ON, L5L 1C6, Canada; Department of Physics, University of Toronto, Toronto, ON, M5S 1A7, Canada; Department of Chemistry, University of Toronto, 80 St. George Street, Toronto, ON M5S 3H6, Canada.

[4] Edmond and Lily Center for Brain Sciences (ELSC), The Hebrew University of Jerusalem, Jerusalem, 91904, Israel.

[5] The Center for Nanoscience and Nanotechnology, The Hebrew University of Jerusalem, Jerusalem 9190401, Israel.

Corresponding authors: eran.meshorer@mail.huji.ac.il; eitan.lerner@mail.huji.ac.il

Abstract

Fluorescent proteins (FP) have revolutionized biology, and are frequently used for studying proteins inside cells. In advanced fluorescence microscopy, FPs might report on additional intracellular variables. One potential variable could be the local density near FPs, which can be useful in studying densities within cellular bio-condensates. Here we show that a reduction in fluorescence lifetimes of common monomeric FPs can report increased levels of local densities. We demonstrate the use of this fluorescence-based variable to report the distribution of local densities within heterochromatin protein 1α (HP1α) in mouse embryonic stem cells (ESCs), before and after early differentiation. We find that local densities within HP1α condensates in pluripotent ESCs are heterogeneous and cannot be explained by a single liquid phase. Early differentiation, however, induces a change towards a more homogeneous distribution of local densities, which can be explained as a liquid-like phase. In conclusion, we provide a fluorescence-based method to report increased local densities and apply it to distinguish between homogeneous and heterogeneous local densities within bio-condensates.

Main

Fluorescent proteins (FPs) are commonly used in fluorescence microscopy for studying protein expression, localization, dynamics, interactions, regulation, and many other biological phenomena by genetic fusion to a protein. The fusion construct facilitates monitoring the localization and dynamic properties of the FP product in living cells. From a structural perspective, FPs include an organic fluorophore formed from a triad of amino acids that react. This fluorophore maturation process occurs inside a β-barrel protein fold, between two α helices crossing the β-barrel from above and below. Additionally, an elaborate network of interactions in the interior of the β-barrel constricts the fluorophore in a well-defined position with minimal degrees of freedom[1–3]. These features render fluorescence intensities from well-folded monomeric FPs as objective reporters of the FP-fused protein concentration.

In any fluorophore, including that in the interior of an FP, fluorescence is a result of a radiative de-excitation pathway, involving the emission of a photon, which competes with a non-radiative de-excitation pathway. The non-radiative de-excitation rate can be influenced by micro-environmental changes in the vicinity of the fluorophore group, among other factors (e.g., temperature, pH). Such factors can be introduced by an increase in the degrees of freedom of the fluorophore within the FP. Since fluorescence lifetime is the inverse of the sum of both de-excitation pathway rates, enhancement of the non-radiative de-excitation rate without changes in the radiative de-excitation rate will lead to reductions in fluorescence lifetime values. Therefore, if increases in local densities of crowdedness in the vicinity of the FP increase the degrees of freedom in the vicinity of the fluorophore inside the FP, then tracking the fluorescence lifetimes of such FPs could be useful in detecting such changes in local densities or crowdedness levels.

Where might such measurements be useful? The typical intracellular crowdedness is estimated at 20-30% fractional volume occupancy (FVO)[4–7]. However, membrane-less bio-condensates that might have undergone phase separation (PS) may exhibit higher densities and hence higher crowdedness levels. For example, the genetic material in living eukaryotic cells is packaged in the form of chromatin, where compaction and expansion of chromatin structure may regulate gene expression and dictate cellular function. In embryonic stem cells (ESCs) and early embryos, chromatin was shown to have a unique open configuration and a hyper-dynamic association with chromatin proteins, including histone proteins and heterochromatin proteins (HP), such as HP1[8–10], a phenomenon also observed in cancer stem cells[11]. The unique conformation of chromatin in pluripotent cells is hypothesized to support pluripotency and cell lineage specifications[12]. In recent years, a growing number of studies emerged, which highlight chromatin as a PS nuclear condensate[13], with liquid-like properties at the nanoscale[14], and solid-like properties at the mesoscale[15]. Studies in yeast and fly demonstrated that liquid-liquid PS (LLPS) of HP1 drives the formation of heterochromatin nano-domains[16,17]. HP1α is commonly

associated with silenced heterochromatin regions[18–20], is highly dynamic[21–24], and is considered a crucial factor in chromatin organization and compaction[25–27]. Moreover, HP1α can form LLPS droplets in different cells and species[16,17,25,26,28]. In mammalian cells, however, HP1α has recently been shown to favor forming condensates via interactions with spatially clustered binding sites (ICBS) without undergoing LLPS[29,30]. Nevertheless, since these studies were performed on differentiated cells, the question remains as to whether HP1 favors forming LLPS- or ICBS-based condensates in undifferentiated cells, especially in pluripotent stem cells, where mesoscale histone dynamics are exacerbated[31]. Recent results show that in undifferentiated ESCs heterochromatin condensates, involving chromocenters, major satellite repeats (MSR) transcripts, and HP1α may be considered to be PS condensates with some features of a liquid phase and others that deviate from a liquid phase[32]. Altogether, the characterization of the biophysical process of HP1α condensate formation in ESCs before and during differentiation is still incomplete.

A general feature of liquid droplets exhibiting a single phase and separated from bulk liquid, much like an oil droplet in water, should exhibit homogeneous density throughout the interior of the condensate, except, perhaps, for its edges[33–35]. Fluorescence-based reporters of local density or crowdedness within a given region of interest (ROI) in an imaged cell could help probe this feature of condensates. Here, we find that significant reductions in the fluorescence lifetimes of monomeric FPs, relative to their typical values, report on densities and crowdedness levels at well-defined FVO values. We show that the reduction of fluorescence lifetime of the FPs due to high levels of crowding occurs due to an increase in the degrees of freedom around the fluorophore in the interior of the FP and by that enhancement of the fluorophore non-radiative de-excitation pathway. We use these methodological developments and employ fluorescence lifetime imaging (FLIM) to study and compare the PS behavior of FP-tagged HP1α in mouse ESCs before and during early differentiation. We demonstrate that HP1α condensates in ESCs exhibit heterogeneous densities that could not be explained by LLPS into a single-phase liquid-like condensate. However, HP1α condensates in retinoic acid (RA)-treated ESCs exhibit densities that are closer to be homogeneous, hence shift towards a liquid-like phase.

Results

Fluorescence lifetime reductions in FPs due to elevated crowdedness levels

To assess the use of fluorescence lifetimes from monomeric FPs for sensing specific physicochemical conditions, we conducted an array of *in vitro* characterizations of such recombinant FPs. We measured mCherry fluorescence decays at different concentrations of: 1) small salt molecules (i.e., NaCl), 2) small viscogen molecules, inducing viscosity but not crowding (i.e., glycerol), 3) small molecules inducing both viscosity and molecular crowding,

acting as protein kosmotropes (i.e., trehalose[36]), and 4) macromolecules inducing both viscosity and macromolecular crowding (i.e., macromolecular crowding agents) of different sizes (e.g., polyethylene glycol, PEG 3,350, PEG 6,000, PEG 10,000[37–39]; Supplementary Fig. 1). We fitted the results to a bi-exponential decay model convolved with the experimental impulse response function (Supplementary equation (1); Supplementary Fig. 2). The best-fit fluorescence lifetime components and their amplitudes were then used for calculating the mean fluorescence lifetimes (Supplementary equation (2)). The results show that different concentrations of NaCl (Fig. 1a) or glycerol (Fig. 1b) do not introduce significant changes or monotonic trends in the values of mean fluorescence lifetimes of mCherry (Fig. 1; Supplementary Table 1). Importantly, the mean fluorescence lifetimes of mCherry in these conditions are around its standard value, 1.4 - 1.6 ns[40,41]. When crowding was introduced, either by the small kosmotrope, trehalose (Fig. 1c) or by the macromolecular crowding agents, polyethylene glycol (PEG) of different sizes (Fig. 1d-f), fluorescence lifetimes of mCherry did not change from its standard value at low concentrations. However, at higher kosmotrope and crowding agent concentrations, the results exhibited a gradual lifetime decrease as a function of concentration (Fig. 1). Converting PEG concentrations to FVO values shows that the gradual reduction in mCherry fluorescence lifetime begins at FVOs of ~30%. To ensure that the observed effect is solely due to changes in fluorescence lifetime, we recorded the steady-state fluorescence spectra of mCherry in these conditions, and the results clearly show that mCherry spectra do not exhibit non-negligible spectral chromatic shifts as a function of the different conditions tested (Supplementary Fig. 3). Importantly, both kosmotropes and macromolecular crowding agents also increase the refractive index in the bulk solution. If the refractive index in the vicinity of the fluorophore inside the β-barrel also increases, that could also a introduce reduction in the fluorescence lifetime, which can be explained by the Strickler-Berg relationship[31]. Interestingly, this effect did not occur in mCherry (Fig. 1b-f) even though the refractive index in bulk solution increases at the tested conditions, possibly because the magnitude of this effect on mCherry was too small to be observed. Encouraged by the results of mCherry, we performed similar analyses for other common monomeric FPs (e.g., mRFP, mCitrine, eGFP), which exhibited similar trends as mCherry, relative to their standard fluorescence lifetime values (Supplementary Figs. 4-6), albeit with different value ranges. Interestingly, eGFP and mCitrine reported fluorescence lifetime reductions from values of ~2.6-2.7 ns[42,40,43] and ~3.4-3.6 ns[44–47], respectively, as a function of both viscosity and crowding (Supplementary Figs. 5-6). Yet, reductions of fluorescence lifetimes of eGFP and mCitrine below the lifetime values at 50% glycerol still occur in the presence of PEG at crowding levels higher than 30% FVO (Supplementary Figs. 5-6). Could it be a result of the refractive index changes on fluorescence lifetime? For PEG 6,000 and similar PEGs, the refractive index reaches an asymptotic value of ~1.46 at an FVO as low as ~5%[48]. Therefore, it is clear that the fluorescence lifetime reductions in eGFP and

mCitrine due to crowding can be separated from the effects due to refractive index changes. Indeed, it has been reported that enhancement of the refractive index leads to reductions in the fluorescence lifetimes of eGFP[49] and mCitrine[50]. All of the physicochemical conditions that were tested induce significant enhancements of the refractive index, including molar concentrations of NaCl. However, such high NaCl concentrations did not induce reductions in monomeric FPs fluorescence lifetimes (Fig.1, Supplementary Figs. 4-6). Nevertheless, even the high NaCl concentrations used here do not introduce increases in bulk refractive index[51] as high as those introduced by PEG[48]. In addition, the lifetime trends observed as a function of PEG are occurring while the bulk refractive index is expected to be almost unchanging[48]. We can therefore conclude that the major reductions in fluorescence lifetimes above a given concentration threshold can be attributed to crowding. Importantly, we can conclude that in mCherry and mRFP, fluorescence lifetime reductions cannot be attributed to changes in bulk viscosity or bulk refractive index, but rather to crowding alone. Similar to mCherry, all other FPs that were tested did not exhibit non-negligible spectral chromatic changes as a function of the different conditions (Supplementary Figs. 7-9).

Mechanism of fluorescence lifetime reduction in FPs

We move to examine the possibility that crowding of the FP from outside, above a given FVO value, could introduce degrees of freedom around the fluorophore group inside the FP, which could enhance the non-radiative de-excitation pathway. If internal degrees of freedom are introduced around the fluorophore, we expect it to exhibit more rotational degrees of freedom relative to the FP β-barrel, as compared to the minimal degrees of freedom the fluorophore has relative to the FP β-barrel in buffer. Since fluorescence anisotropy decays track different types of rotational movements of a given fluorescent system, it can capture such effects[52]. This is mainly because the rotational correlation times of the fluorophore itself relative to the FP to which it is linked should be faster than the whole FP tumbling rotational correlation time.

We performed time-resolved fluorescence anisotropy measurements of mCherry (Fig. 2a-b) in 1) 0% FVO PEG 6,000 (buffer only), 2) in 25% FVO PEG 6,000, where only the increased viscosity is expected to slow down motions and fluorescence lifetime does not yet change (Fig. 1e), and 3) in 50% FVO PEG 6,000, where viscosity is further increased, and fluorescence lifetime decreases (Fig. 1e), but potentially also the internal degrees of freedom of the fluorophore relative to the FP β-barrel increase (Fig. 2a, red, Fig. 1b). The fluorescence anisotropy decay was then calculated from the polarized fluorescence decays (Supplementary equation (3)). Since the fluorophore system is constricted inside the FP, it is expected that mCherry in buffer will exhibit a fluorescence anisotropy decay with mostly a slow decaying component representing the slow tumbling of the whole FP (Fig. 2b, black). On the other hand, the enhancement of internal degrees of freedom in the vicinity of the fluorophore due to

crowding on the exterior of the FP should introduce, aside from this slow protein tumbling process, another faster-decaying term (Fig. 2b, green). Note that this fast-decaying component appears at PEG above 30% FVO, above which the lifetime reduction starts to occur in mCherry (Fig. 1d-f). However at 25% FVO, below the 30% cutoff, it seems that the effect of viscosity slowdown of protein tumbling is the only effect that occurs (Fig. 2b, red). We conclude that above the 30% FVO of PEG fluorescence lifetime reduction is correlated with an enhancement of the rotational degrees of freedom of the fluorophore group relative to the FP β-barrel.

To provide an atomistic explanation for fluorescence lifetime reduction caused due to macromolecular crowding by elevated FVO of PEG, we performed extensive MD simulations of mCherry in solution both in the absence of PEG and in the presence high %FVO of PEG, calculated to be 42% (e.g., >30% FVO PEG; Fig. 3a-b), for a combined total of 20 μs. The fluorophore participates in a network of fluctuating contacts with many residues in the protein (Supplementary Table 2). We refer to this network of residues as the fluorophore pocket. Additionally, we observe that water molecules are found within the pocket (Fig. 3c). The volume of the pocket fluctuates over the course of the simulation, and since water molecules are easier to displace than protein residues, the volume of the pocket can be used as a proxy for the flexibility of the fluorophore's environment. Therefore, to quantify the rigidity of the fluorophore's environment, we computed the volume of the fluorophore pocket, and show the distribution of pocket volumes for each system (Fig. 3d). The distribution of fluorophore pocket volumes in the presence of 42% FVO PEG is shifted significantly to larger volumes relative to the distribution in the absence of PEG, indicating that the fluorophore pocket has a larger volume on average under high levels of crowding. This shift in pocket volume suggests that interactions with PEG lead to a protein conformation in which there is more space in the vicinity of the fluorophore, and therefore room for more flexibility in the fluorophore's environment.

To further investigate the potential conformational basis of the pocket volume increase, we computed the average pairwise distances of the pocket residues (Fig. 3f). We observe that in the presence of 42% FVO of PEG, most pocket residues inside the β-barrel of mCherry have increased distance from each other, indicating a global expansion of pocket residues inside the β-barrel. Despite this difference in fluorophore pocket size, we observe no significant difference in hydrogen bonds between the fluorophore and the rest of the protein (Supplementary Fig. 10), consistent with the observation that absorption and emission spectra are unaffected by PEG[53]. Finally, the position of the central helix in mCherry differs in the presence of PEG relative to in the absence of it. Conformations in which the helix is farther from the β1-β5 and closer to the β7-β10 gap region are preferred (Fig. 3e-f). The β7-β10 gap is known to be a flexible part of mCherry[54]. Taken together, these results are consistent with the hypothesis that crowding mCherry from outside the β-barrel reduces the fluorescence lifetime of mCherry by inducing a

conformational change that reduces the protein constraints on the fluorophore, increasing the rate of non-radiative de-excitation.

Following these results, we proposed to probe whether other residues that point towards the interior of the FP β-barrel, such as its three Trp residues (i.e., residues 58, 93 & 143), also experience the change in the interior of the FP due to crowding from its exterior. Note that while Trp93 and Trp143 are in the vicinity of the fluorophore (i.e., in direct contact 100% and 30% of the simulation snapshots, respectively), Trp 58 is not, yet is still part of the interior environment. We chose Trp since it can be selectively excited, and its fluorescence spectra can report on changes in their vicinities. The results of Trp fluorescence spectra measurements as a function of different FVO values of PEG report on an overall quenching transition occurring at 20-30% FVO PEG (Fig. 2c, Fig. 2e, black), with a gradual moderate blue shift of the wavelength of maximal fluorescence, λ_{max}, from 25% FVO and above (Fig. 2d, Fig. 2e, red). These results are correlated with the increase in the degrees of freedom in the FP interior. Indeed, the MD simulations report on a slight increase in solvent accessibility for Trp58 in the presence of high levels of PEG relative to when it is solely in water (Supplementary Fig. 11a-c). Additionally, the MD simulations reports on subtle C_α-C_α distance changes between the Trp residues and their neighboring residues (Supplementary Fig. 11d-f), which could also explain the Trp fluorescence changes in terms of changing Trp immediate chemical environment.

Utilizing FLIM to measure fluorescence lifetime reduction of FP precipitates

Reduction in the fluorescence lifetime of mCherry relative to its standard value can be used in FLIM to report on regions in a fluorescently imaged object with high local densities caused by crowding of at least 30% FVO. However, we were not able to continue the assessment of fluorescence lifetimes in bulk solution above 50% FVO of PEG. If so, how can we probe the continuation of the fluorescence lifetime reduction at % FVO of PEG higher than 50%? One way would be to measure mCherry lifetimes in its precipitates. Increased levels of PEG and protein mixtures form precipitates, where the concentrations of the constituents are larger than in bulk solution[55–57]. We can therefore probe fluorescence lifetimes of FPs in these precipitates, and expect even more reduction of fluorescence lifetimes in them relative to the fluorescence lifetimes in the bulk solution. Therefore, we performed a controlled test on PEG-induced precipitates, which were formed after mixing 100 nM mCherry with increasing PEG 6,000 FVO values (Fig. 4b,d). Then, we performed FLIM on the precipitates that accumulated on the surface of the coverslip (Fig. 4a,c,e; Supplementary movies). Without PEG and in the presence of PEG at 10% FVO, there was no sign of fluorescent precipitates accumulating at the surface of the slide. Fluorescent precipitates appeared in the presence of PEG at 25% FVO, and at 50% FVO multiple µm-size precipitates were observed immediately upon preparation (Fig. 4b,d). The fluorescence images of precipitates exhibit interesting characteristics: 1) irregular shapes

(Fig. 4a), 2) different precipitates with different fluorescence lifetimes (Fig. 4a,c,e), 3) fluorescence lifetimes within precipitates are rather uniform per image frame (Fig. 4a,c), and 4) the fluorescence lifetimes within precipitates change dynamically from one frame to the next (Fig. 4e; Supplementary Movies), and hence the precipitates exhibit dynamic changes in their densities. Importantly the fluorescence lifetime values of mCherry in precipitates at bulk FVO >25% were ~1.10-1.25 ns, values that in bulk solution represent PEG at 40% FVO or higher (Fig. 1). Alternatively, at 25% FVO of PEG, in bulk solution no fluorescence lifetime reduction is expected (Fig. 1), however, because the concentrations in precipitates are higher than in bulk solution, we observed reduction in fluorescence lifetime even when we introduce 25% FVO into the bulk.

Taken together, when performing FLIM of monomeric FPs, such as mCherry, fused to specific proteins, fluorescence lifetimes lower than their standard values can report on local densities or crowdedness per pixel of an image, under the assumption that crowdedness is at least above a given threshold. With this approach, we next characterize HP1α heterochromatin-associated condensates in differentiating pluripotent mouse embryonic stem cells (ESC) using FLIM.

The phase of HP1α condensates in undifferentiated and early differentiated ESCs

Significant changes in chromatin compaction and nucleosome plasticity occur during ESC differentiation[58], and nucleosome plasticity was shown to drive chromatin PS properties[59]. HP1 binding to heterochromatin and forming domains or condensates around it renders HP1 a crucial factor in heterochromatin structure. Despite several studies reporting different physical mechanisms underlying HP1α condensates[16,17,20,21,23,24,26,27,29], the basis of their formation in undifferentiated ESCs and during early differentiation is still obscured and has just started to be explored[32]. We, therefore, set out to study HP1α condensates before and after early ESC differentiation.

We performed FLIM of mCherry-fused HP1α, taking advantage of our previously-generated endogenously-tagged mCherry-HP1α fusion ESC clones[60,61], and report on the mCherry fluorescence lifetimes within these condensates. Despite the high mobility of HP1α throughout the nucleus[8,11], it forms stable condensed heterochromatin structures, which are actively renewed, as has been previously shown[21,22]. By using in-cell fluorescence correlation spectroscopy (FCS) measurements inside HP1α foci (Supplementary Fig. 12; equations (4, 5))[62] and following photobleaching rate analyses (Supplementary Fig. 13; equation (6)), we confirm that HP1α retains its mobility inside the condensates, and therefore exists in a liquid-like phase and is actively renewed. Next, we compared images of fluorescence intensity and FLIM of endogenously-tagged mCherry-HP1α ESC clones that grew either as undifferentiated ESCs or following two days of retinoic acid (RA)-induced differentiation, referred to here as early differentiated ESCs. While in the fluorescence images the intensities within condensates are

rather homogeneous (Fig. 5), the shapes of these condensates in undifferentiated ESCs tend to deviate from the circular and symmetrical shapes expected of LLPS condensates with an interior single liquid phase (Fig. 5a-d). However, after early differentiation, the shapes of the observed HP1α foci are smaller and more symmetric (Fig. 5e-h). Additionally, while in undifferentiated ESCs there are only a few large condensates in each nucleus, after early differentiation cells display many smaller-sized condensates per nucleus, as previously reported[8,63].

The interior of a LLPS-induced condensate composed of an interior single liquid phase is expected to exhibit uniform density. Therefore, if mCherry-HP1α condensates formed through classic liquid-liquid phase separation induced by crowding of >30% FVO, we expect to observe a homogeneous (i.e., single population) distribution of fluorescence lifetimes within all pixels of the condensate. On the contrary, our results show a varying range of fluorescence lifetimes in the interiors of HP1α condensates in undifferentiated ESCs (Fig. 5a-d). These condensates exhibited sub-domains with lifetime values <1.44 ns, below which >30% FVO PEG has shown to initiate the lifetime reduction trend (Fig. 1). Therefore, FLIM of mCherry-HP1α shows that in undifferentiated ESCs it cannot be described by LLPS condensates with an interior single liquid phase. Importantly, these condensates cannot be represented by a solid phase either, since they exhibited mCherry-HP1α diffusivities within them, which should be abolished in a solid phase (Supplementary Fig. 12). These results are in line with HP1α condensates in mouse ESCs that (i) adopt a mobile yet non-liquid phase (e.g., gel-like), (ii) contain multiple sub-domains, each with its liquid phase and density, or (iii) cannot at all be described as a PS condensate.

Having established that undifferentiated ESCs display heterogeneous fluorescence lifetimes (Fig. 5a-d), as ESCs undergo early differentiation induced by RA, an increasing number of condensates shift towards longer fluorescence lifetimes with less heterogeneity of values across imaged condensates (Fig. 5e-h). These results indicate a transition upon ESC differentiation towards condensates that are less dense and with a more homogeneous density, hence a result that is more consistent with a LLPS-induced condensate with an interior single liquid phase.

While these results refer to the distribution of fluorescence lifetimes within HP1α condensates, examination of mean fluorescence lifetimes between multiple HP1α condensates in multiple image acquisitions is necessary to explore the generality of the identified phase behavior and how it might distribute across multiple cells and image acquisitions. Therefore, we quantified mCherry fluorescence lifetimes of multiple condensates from multiple image acquisitions, and compared them against the mean fluorescence lifetime values outside the condensates (Fig. 6). The results report on the following trends: 1) in undifferentiated ESCs, the heterogeneity in fluorescence lifetimes in HP1α condensates distribute in at least two major sub-populations, both with lower values than the typical fluorescence lifetime value of mCherry (Fig. 6, dashed red line); 2) fluorescence lifetimes in HP1α condensates after early differentiation distribute in

a major single population, similar to the higher lifetime sub-population undifferentiated ESCs. These results indicate that the mean densities of HP1α condensates are higher than the FVO threshold above which fluorescence lifetime reductions are observed (Fig. 1), but also point towards more heterogeneity in densities in undifferentiated ESCs than in early differentiated ones not only within but also between HP1α condensates.

In summary, these results show that HP1α can accumulate in intranuclear condensates exhibiting diffusional mobility yet not necessarily single-liquid phase in undifferentiated ESCs, and that gradually shift to a phase with features closer to a liquid upon induction of early differentiation conditions.

Discussion

In this work, we have shown that fluorescence lifetime reduction in FPs can serve as a reporter of increased local densities or crowding levels. The results of the herein methodological developments warrant using FLIM to assess local densities of FP-fused proteins in cellular regions that experience high molecular densities, such as those found in small cellular compartments and in PS condensates.

There are many useful fluorescence-based approaches for studying the properties of PS condensates in the cell through measuring diffusivities, e.g., by in-cell FCS[64,65], or fluorescence recovery after photobleaching[29,66], through tracking fluorescence intensity images to capture condensate fusion and fission events[17] or by characterizing condensate circularity[17]. A key feature of LLPS condensates having an interior single liquid phase is the uniform density that is to be expected in the interior of a condensate, and hence heterogeneities in crowding are not expected. Therefore, a fluorescent reporter of local densities or crowdedness levels is necessary to characterize the actual physical phase of biomolecular condensates. Such fluorescent-based reporters of crowding were previously developed based on FRET between two FPs fused through a crowding-sensitive protein[67,68]. However, FRET-based crowding probes require using two spectrally-separated FPs, which reduce the spectral ranges available for imaging of other fluorescently-tagged targets in the cell. Additionally, since these FRET crowding sensors do not localize solely inside bio-condensates of choice, they might not necessarily provide contrast to distinguish between the interior and exterior of cellular condensates. It is noteworthy that fluorescence intensity, even for single FPs, does not necessarily scale only as a function of the number of FPs within an image pixel, but is also influenced by fluorescence quantum yields and lifetimes. Accordingly, we propose using FLIM to image proteins genetically fused to typical monomeric FPs that exhibit fluorescence lifetime reductions mostly in response to increased density and crowding above a given FVO threshold, to report on local densities inside PS condensates. Density heterogeneities within PS condensates may imply a deviation from the single-liquid phase scenario, which together with findings from other methods could enable a

more complete physicochemical characterization of the condensates under study. Importantly, since this approach is not specific to PS condensates, it may be used in other applications of cellular imaging with high levels of crowding.

Unlike mCherry and mRFP, our measurements show that the fluorescence lifetimes of eGFP and mCitrine may be influenced not only by crowding but also by an increase in the refractive index near the fluorophore inside the β-barrel. This effect is established in the Strickler-Berg relationship between the rate of radiative de-excitation of the fluorophore and the square of the refractive index in the vicinity of the fluorophore, and hence depends inversely on the fluorescence lifetime. We have shown that this effect occurs mostly in green-yellow fluorescent proteins (e.g., eGFP, mCitrine; Supplementary Figs. 5, 6), and it was most probably due to their lower structural stability relative to the red fluorescent proteins (e.g., mCherry, mRFP), where this effect was negligible[69]. Therefore, we propose to use fusions of mCherry, mRFP, or other monomeric FPs that exhibit fluorescence lifetime reductions mostly or solely due to crowding. Additional monomeric FPs designed to be highly stable have been reported in the literature[70] and are potential subjects for further investigations similar to those presented here.

We have demonstrated that crowding, acting from outside the FP, increases the volume of the fluorophore pocket inside the FP, and that, in turn, increases the degrees of freedom around the fluorophore, which lead to an enhancement of the non-radiative de-excitation pathway of the fluorophore, and hence to fluorescence lifetime reduction. These results could explain why above 30% FVO of PEG the fluorophore exhibits rotational degrees of freedom relative to the FP, which did not show up below that FVO value. What could be the photophysical mechanism behind the increased degrees of freedom around the fluorophore leading to the enhancement of its non-radiative de-excitation pathway? A closer look at the molecular structure of FP fluorophores could suggest that if they were not spatially restricted by the FP barrel, they would have undergone *cis-trans* photoisomerization, between isomers that emit photons upon de-excitation and isomerization intermediates, which do not emit photons upon de-excitation[71]. This way, since with no spatial constrictions photo-isomerization is very efficient[72–75], the overall fluorescence quantum yield would be low. Since the fluorophore is constricted within the FP, it can be assumed that its photoisomerization is limited, and hence that its fluorescence quantum yield is optimized, if not maximized. Nevertheless, if the degrees of freedom around the fluorophore increase and allow some degree of fluorophore photoisomerization, this will decrease the fluorescence quantum yield, and hence also the fluorescence lifetime. Indeed, inhibition of *cis-trans* photoisomerization has been shown to occur in FP fluorophores when free in solution[71,76–78]. This characteristic of FPs is useful when mutationally designing FPs that undergo fluorescence blinking, by altering the spatial constriction of the fluorophore[78] for applications such as single-molecule localization microscopy[79,80]. Nevertheless, there could also be uses for FPs that exhibit high spatial restriction of their fluorophores to sense local

environmental effects. Finally, while modulation of *cis-trans* photoisomerization is one way of facilitating fluorescence lifetime reductions upon enhancement of degrees of freedom in the interior of an FP, other photophysical mechanisms can induce fluorescence lifetime reduction upon such degrees of freedom increase. Additionally, other factors complicate the search for the underlying mechanism. For instance, FP fluorophores exhibit different ionic forms as a function of pH, which could induce dramatic changes to their fluorescence characteristics[81]. Therefore, it is important to use FPs that have low pKa values, such as mCherry[82], and perhaps focus on imaging cellular compartments that do not exhibit large pH deviations from neutral values, such as in the nucleus.

To explore the utility of this method, we employed FLIM to assess the PS properties of HP1α in heterochromatin condensates in undifferentiated and early differentiating mouse ESCs. We used our endogenously-labeled mCherry-HP1α ESCs[60,61], to evaluate the fluorescence lifetimes in heterochromatin foci in both undifferentiated ESCs and in RA-treated ESCs for two days to capture the very early stages of differentiation. This non-invasive approach for monitoring protein condensation enabled us to identify heterochromatin protein reorganization processes inside of the foci in pluripotent and early differentiated cells. Previous work from us and others revealed increased chromatin protein dynamics in heterochromatin of pluripotent versus differentiated cells, where this dynamic association with heterochromatin is restricted[8–10,83–85], and several studies began to identify some of the underlying mechanisms, including specific factors[84], or chromatin-lamina interactions[9].

Here we tested whether the PS properties of heterochromatin may explain these previous observations. Intriguingly, we identified an early transition from a relatively heterogeneous distribution of fluorescence lifetimes in heterochromatin foci of undifferentiated ESCs to a more homogeneous state in the RA-treated ESCs, with an increasing number of foci entering longer and more homogeneous distribution of fluorescence lifetimes. The main difference we previously observed in HP1 dynamic association with chromatin between undifferentiated and early differentiated ESCs was the bleach depth[8], indicating that undifferentiated ESCs possess an additional sub-population of highly dynamic HP1 molecules, in addition to the one observed in early differentiated ESCs. This sub-population coincides with the increased density heterogeneity within the condensates we studied here in undifferentiated ESCs, but not in early differentiating cells. Our observations could be explained by a model of HP1 foci with different liquid subdomains, each phase-separated within the foci themselves, and with its distinct dynamics. This would explain both the larger heterogeneity we observe within undifferentiated ESCs and the transition from this heterogeneous multi-subdomain state into a more homogeneous liquid-like state in early differentiation. Indeed, several works have shown that HP1α condensates exhibit behavior that cannot be explained by a liquid phase, at least partially[17,21,28]. Recently, Novo *et al.* demonstrated that heterochromatin condensates,

comprising MSR transcripts and HP1α, form in undifferentiated mouse ESCs[32]. Interestingly, these condensates exhibited features that can be partially explained as induced by LLPS towards an interior single liquid phase and others that cannot (e.g., irregular shapes, substantial immobile fraction), and hence coincide with the heterogeneities we report here. Interestingly, upon MSR transcript depletion, the heterochromatin condensates exhibited characteristics of homogeneous condensates. Indeed, we have previously shown that ESC differentiation leads to the depletion of such noncoding satellite repeat transcripts[86], and hence the Novo *et al.* findings coincide also with our own regarding early differentiated mouse ESCs.

While we report a new methodological concept and demonstrate its use, many questions are yet to be answered. On the FP side, how many other FPs can also exhibit the effects shown here by mCherry and mRFP? Could the reported crowding effects on internal fluorophore degrees of freedom be mutationally designed? On the application of FPs to study PS condensates, what further phase transitions could be studied with this approach combined with other experimental approaches? and most importantly, could the herein presented experimental approach assist in achieving a clear picture of PS condensates in cells? We envision these questions as well as others would be answered down the road in future studies building on this work.

Methods

Expression and purification of recombinant His6 tagged monomeric FPs

BL-21 competent cells were transformed using mCherry, eGFP, mRFP[87], and mCitrine plasmids acquired from addgene as a gift from Michael Davidson, Robert Campbell, Roger Tsien or Scott Gradia (addgene plasmid mCherry: #29722, eGFP: #54762, mRFP: #54667 and mCitrine: #29724). A single colony of transformed BL-21 cells was inoculated in 10 mL of LB media supplemented with 100 µg/mL Ampicillin or 50 µg/mL Kanamycin and incubated overnight at 37˚C and 250 rpm. The overnight culture was diluted (1:100, v:v) into a new autoclaved 2 L Erlenmeyer with 1 L LB media supplemented with 100µg/mL of the appropriate antibiotic. Culture growth was monitored by periodically measuring OD_{600}. Once OD_{600} reached 0.6 (~4 hrs after inoculation) culture was induced with 1 mL of 1 M IPTG (to final concentration of 1 mM) for mCherry and mCitrine or with 2% arabinose for eGFP and mRFP, and continued incubation for another 3 hrs. Cells were harvested by centrifugation at 6000 g and 4 ˚C for 10 min using 250 mL bottles in R12A3 rotor and Hitachi Koki himac CR22N high-speed refrigerated centrifuge. Pellets were stored at -80 ˚C. Pellets from 1 L cell media were resuspended in 50 mL of lysis buffer (100 mM sodium phosphate, 100 mM NaCl, pH 7.0), and lysed by ultra-sonication (10-12 cycles of 20 s pulses with 50 s intervals, at 60% amplitude). Cell debris was removed by centrifugation at 12,000 rpm, 4 ˚C for 30 min. HisTrap HP 1mL was used to separate the his-tagged FPs from the supernatant using the AKTA system[886]. Fractions collected were run in SDS-PAGE to assess the purity of the protein. Pure fractions

were dialyzed overnight in dialysis buffer (20 mM Na2HPO4, 50 mM NaCl, pH=7.8) and stored in 50% glycerol at -20 ˚C.

ESC culture and differentiation

ESCs were cultured on 0.2% gelatin-coated plates and grown on a feeder layer of mitomycin C-treated mouse primary embryonic fibroblasts (MEFs) and maintained in ESC media (DMEM, 10% FBS, 1000U of leukemia inhibitory factor [LIF], 2 mM L-glutamine, 1% nonessential amino acids, 50 units/ml penicillin, 50 μg/ml streptomycin and 0.1 mM β-mercaptoethanol). Cell cultures were maintained in a humidified atmosphere (5% CO2 at 37˚C). For RA-induced differentiation, ESCs were grown on gelatin-coated dishes without MEFs for up to 2 days in ESC medium without LIF and with 1 μM RA. For cell live imaging, cells were seed on an ibiTreat 8-well μ-Slides (#80826 ibidi, Munich, Germany) in appropriate cell culture medium and conditions.

Experimental setup for FLIM, fluorescence lifetime, FCS and time-resolved fluorescence anisotropy measurements

We performed fluorescence lifetime imaging (FLIM) and in-cell fluorescence correlation spectroscopy (FCS) using a confocal-based microscopy setup (ISS^{TM}, Champaign, IL, USA) assembled on top of an Olympus IX73 inverted microscope stand (Olympus, Tokyo, Japan). We used 532±1 nm pulsed picosecond fiber laser (FL-532-PICO, CNI, China; pulse width of 100 ps FWHM, operating at 20 MHz repetition rate and 100 μW, measured at the back aperture of the objective lens) for exciting mCherry-HP1α. The laser beam passes through a polarization-maintaining optical fiber (P1-405BPM-FC-Custom, with specifications similar to those of PM-S405-XP, Thorlabs, Newton, NJ, USA) and after passing through a collimating lens (AC080-016-A-ML, Thorlabs), the beam is further shaped by a linear polarizer (DPM-100-VIS, Meadowlark Optics, Frederick, CO, USA) and a halfwave plate (WPMP2-20(OD)-BB 550 nm, Karl Lambrecht Corp., Chicago, IL, USA). A major dichroic mirror with high reflectivity at 532 and 640 nm (ZT532/640rpc, Chroma, Bellows Falls, Vermont, USA), for mCherry, and at 488 and 640 nm (ZET488/640m, Chroma, Bellows Falls, Vermont, USA), for GFP, reflect the light to the optical path through galvo-scanning mirrors (6215H XY, Novanta Corp., Boston, MA, USA) and scan lens (30 mm Dia. x 50mm FL, VIS-NIR Coated, Achromatic Lens, Edmund Optics, Barrington, NJ, USA; both used to acquire the scanned image), and then into the side port of the microscope body through its tube lens, positioning it at the back aperture of a high numerical aperture (NA) super apochromatic objective (UPLSAPO100XO , 100X, NA=1.4, oil immersion, Olympus), which focuses the light onto a small effective excitation volume, positioned within the sample chamber (μ-Slide 8 Well high Glass Bottom, Ibidi, Gräfelfing, GmbH). Scattered light returns in the excitation path, and a

fraction of it is imaged on a CCD camera, used z-positioning, using Airy ring pattern visualization. Fluorescence from the sample is collected through the same objective, is transmitted through the major dichroics and is focused with an achromatic lens (25mm Dia. x 100mm FL, VIS-NIR Coated, Edmund Optics) onto a 100 µm diameter pinhole (variable pinhole, motorized, tunable from 20 µm to 1 mm, custom made by ISS™), and then re-collimated with another achromatic lens (AC254-060-A, Thorlabs). Fluorescence is then further cleaned using a 615/24 nm, for mCherry, or 510/20 nm, for eGFP, single band bandpass filter (FF01-615/24-25, or FF01-510/20-25, Semrock, Rochester, NY, USA). Fluorescence was collected using one hybrid PMT, routed to a TCSPC card (SPC 150N, Becker & Hickl, GmbH). Images were attained by using a laser scanning module (LSM), in which a 3-axis DAC module (custom made by ISS™) synchronized the data acquisition and control over the x & y galvo-scanning mirrors, which assisted in bringing the effective excitation volume to different positions to acquire pixel data per a given z layer. For *in vitro* FLIM measurements, lifetime images were attained by tail fitting the mCherry fluorescence decays of each acquire pixel, if it had at least 30 photons, where the scanning conditions are pixel dwell time –0.1 ms; number of pixels 256x256; field of view area –50x50 5 µm; number of acquired frames per image – 5. Data acquisition is performed using the VistaVision software (version 4.2.095, 64-bit, ISSTM) in the time-tagged time-resolved (TTTR) file format.

In FLIM, lifetime images were attained by tail fitting the mCherry fluorescence decays of each acquire pixel, if it had at least 150 photons. Tail fitting was performed using a sum of two lifetime components function, and the intrinsic mean lifetimes were reported. For retrieving mean fluorescence lifetime values of bulk fluorescence decays of recombinant mCherry, we performed a fitting procedure, with equation (1) and (2) (see in Supplementary Information), as explained in the text, using a Fortran-based software from Haas and colleagues[89,90]. Measurements were performed in PBS buffer (50 mM NaH_2PO_4, 100 mM NaCl, 30mM KCl, pH=7.0) at 100 nM protein concentration.

Time-resolved fluorescence anisotropy measurements (i.e., fluorescence anisotropy decays) were performed by adding a polarizing beam-splitter between two detectors, where one detector reports on fluorescence in a polarization parallel to that of the excitation polarization, and the other perpendicular to the excitation polarization. It is noteworthy that in the setup, the excitation is conditioned so that it reaches the sample with a vertical polarization. Then, fluorescence decays in the polarization parallel and perpendicular to the excitation polarization were recorded. The fluorescence anisotropy decay was calculated out of the fluorescence decays, after 1) correcting the perpendicularly polarized decay relative to the parallel polarized decay with a G factor, and after 2) one decay was shifted relative to the other by the time interval between them, which is due to the slightly different light path lengths for the two detectors. Overall, the anisotropy decay was calculated as in Supplementary equation (3). These

measurements were performed on mCherry at 100 nM concentration in the PBS buffer mentioned above. Using free dye, we measured the expected G factor which was used in calculating the anisotropy. For further explanations, see Supplementary Information.

In-cell FCS was performed by positioning the laser focus at a given point within a ROI and recording the fluorescence trajectory at this point for 2 min. The fluorescence trajectories typically exhibited a monotonic decay of fluorescence due to photobleaching. Next, the fluorescence autocorrelation function was calculated from the acquired fluorescence trajectories (Supplementary equation (4)), as previously shown[64,65]. The fluorescence autocorrelation functions were fitted to a model that includes two modes of translational 3D diffusion, with different fractions (Supplementary equation (5); see Kim, Heinze & Schwille[65]). This model was chosen after we found that it improved curve fitting relative to the fitting of a model with a single 3D diffusion species. Since one diffusion time component included values that do not make sense for measuring 3D diffusion in the cell (i.e., few ms or faster that equate to free organic dyes), we report the diffusion times of the slow component, which are also representative of the fluorescence autocorrelation functions (see Supplementary Fig. 12b).

To characterize the fluorescence photobleaching rates in the in-cell fluorescence trajectories acquired, we fitted them to a bi-exponential decay model (Supplementary equation (6)), as is performed in other similar studies[91,92] (Supplementary Fig. 13). Importantly, the timescale of fast and slow photobleaching are slower than the timescales reported in the FCS fluorescence autocorrelation curves. Therefore, it can be assumed that the FCS analyses were of diffusion-driven fluctuations that occur faster than photobleaching rates, and hence are not influenced by the photobleaching. Therefore, the FCS analyses results for the diffusion times are reliable. On the other hand, due to the ever-decreasing fluorescence, and hence and ever decreasing number of fluorescent molecules in the laser focus, the FCS analyses results for the mean number of molecules free parameter are unreliable. In addition, the results of the analyses of photobleaching rates carry additional information regarding diffusion: while slowly diffusing species stay for longer dwell times within the laser focus, and hence exhibit a higher probability to undergo photobleaching, rapidly diffusing species stay short dwell times within the laser focus, and hence exhibit lower probabilities to undergo photobleaching. In short, while the fast-decaying component of the photobleaching can report on slowly diffusing species, the slow decaying component can report on faster diffusing species. We therefore report the results of the photobleaching decay analyses (Supplementary Fig. 13).

Trp fluorescence spectra

Trp fluorescence spectra of mCherry in the absence and presence of different FVO levels of PEG were recorded using a spectrofluorometer (Jasco FP8200ST, Japan), scanning emission wavelengths in the range 305-400 nm and focusing on excitation at λ=295 nm.

Molecular Dynamics Simulations

System Setup & Simulation Protocol:

The crystal structure of mCherry was taken from the Protein Data Bank (PDB ID 2H5Q)[1]. Missing atoms were added with CHARMM-GUI PDB-reader tool[93]. Missing residues at the termini and a six residue histidine-tag at the C-terminus were added with CHIMERA[94] and their structures were modeled with the MODELLER loop refinement tool[95]. Five structures were generated and the one with the lowest discrete optimized protein energy score[96] was used as the initial structure for MD simulations.

All simulations were performed in GROMACS version 2022.2[97,98]. The mCherry anionic fluorophore parameters[99] were converted to GROMACS format using the charmm2gmx python script with some modifications for Python3 compatibility. The CHARMM36m force field[100] was used with the CHARMM-modified TIP3P water model[101]. The N- and C-termini were protonated in the charged state and all titratable residues were simulated in their standard states for pH 7. For the simulations of the protein in water, the protein was positioned in a triclinic box with 10 Å distance to all box edges. Periodic boundary conditions were used. Water molecules were added to the simulation box and neutralizing Na^+ and Cl^- ions were added at a concentration of 139.7 mM. Energy minimization was performed using the steepest descent method. The system was equilibrated for 10 ns in the NVT ensemble with 1,000 kJ/mol position restraints on all protein heavy atoms. The v-rescale thermostat[102] was used and velocities were generated from a Maxwell distribution. This was followed by a 10 ns constant pressure simulation using the Berendsen barostat[103] and the v-rescale thermostat[102], without changing the position restraints. The Parrinello-Rahman barostat[104] and the v-rescale thermostat[102] were used for all subsequent simulations. Next, the system was equilibrated for 20 ns in the NPT ensemble without changing the position restraints. The system was then equilibrated without any position restraints for 100 ns. Finally, five replicate production simulations were run for 2 μs in the NPT ensemble. A time step of 2 fs was used for all simulations. The bonds involving hydrogen atoms were constrained using the LINCS algorithm[105] and water molecules were constrained using the SETTLE algorithm[106]. Short-range electrostatic interactions and van der Waals interactions were computed with a cutoff of 12 Å. Long range electrostatics were computed using Particle Mesh Ewald summation[107] with 16 Å grid spacing and fourth order interpolation. The Verlet cutoff scheme was used for neighbor searching. The temperature was maintained at 298 ^{o}K, and the pressure was maintained at 1 bar.

A PEG-water system with 200 PEG 28-mer molecules and 6,184 water molecules was set up using CHARMM-GUI[93] polymer-builder tool. The energy of the system was minimized using the steepest descent method. The initial equilibration of the system was carried out using the MD parameter file provided by CHARMM-GUI, which specified the Nose-Hoover

thermostat[108]. This equilibration was run in the NVT ensemble for 250 ps, followed by a 1 ns equilibration simulation in the NPT ensemble using the Parrinello-Rahman barostat[104]. This was followed by a 100 ns equilibration simulation in the NPT ensemble using the v-rescale[102] thermostat and the Parrinello-Rahman barostat[104]. Six random conformations of PEG were selected from the final frame of this simulation and were used for setting up the protein-water-PEG system. The pre-equilibrated structure of mCherry from the simulations in water was used for initial setup of the PEG system. All water molecules and ions were removed. PEG molecules were inserted into the simulation box using the GROMACS tool gmx insert-molecules. Water molecules were then added to the system along with neutralizing Na^+ and Cl^- ions at a concentration of 139.7 mM, for a final PEG concentration of 42% FVO. The energy of the system was minimized using the steepest descent method. The simulations then followed the same protocol as in the system without PEG (see above).

Analysis of Simulation Trajectories:

The first quarter of each simulation was treated as an equilibration period and omitted from all analyses on the basis of radius of gyration, number of hydrogen bonds, and root mean squared deviation. All coordinate-based trajectory analysis was performed using the MDAnalysis module version 2.2.0[109] for Python3. Residues were classified as fluorophore pocket residues if they formed contacts with the fluorophore in more than a 0.33% of all simulation snapshots in each system. Residues were classified as Trp pocket residues if they formed contacts with each Trp in at least 0.33% of simulation snapshots. Two residues were considered to be in contact if any of their atoms were within a distance cutoff of 3.5 Å. Pocket volumes were defined as the convex hull volume of all C_α atoms in the pocket residues. The convex hull was determined with the Open3D[110] module for Python3 after extracting the atomic coordinates using MDAnalysis[109]. Hydrogen bonds were computed with MDAnalysis version 2.2.0 using a distance cutoff of 3.5 Å and an angle cutoff of 150°. Uncertainty is reported as the standard error of the mean, with each independent trajectory being treated as an independent measurement.

Acknowledgements

This project was supported by the Israel Science Foundation (grant 556/22 to E.L.; grant 3565/20 to E.L., within the KillCorona – Curbing Coronavirus Research Program) and the European Union's Horizon Europe Research and Innovation Programme under the EIC Pathfinder-Open grant agreement #101099654 (*RT-SuperES* to E.M.). E.M. is the incumbent of the Arthur Gutterman Professor Chair for Stem Cell Research. This research was supported by a Natural Sciences and Engineering Research Council of Canada of Canada (NSERC) Discovery Grant to S.R. and computational resources provided to

S.R. by Calcul Québec (calculquebec.ca) and the Digital Research Alliance of Canada (alliancecan.ca).

Author Contributions

K.J. and S.D. produced and purified recombinant monomeric FPs, K.J. performed fluorescence spectra and lifetime characterizations and FLIM of monomeric FP precipitates for all recombinant monomeric FPs, as well as mCherry fluorescence anisotropy decays and Trp fluorescence spectra, both acquisition and analyses, L.H-N. and S.R. designed, performed and analyzed all atom explicit solvent molecular dynamics simulations, J.O.V. performed ESC-related experiments, J.O.V., P.S.L.L., S.B. & P.D. performed confocal microscopy acquisitions of ESCs. S.B. and E.L. analyzed the fluorescence lifetimes of FLIM images and P.S.L.L. and E.L. analyzed the in-cell FCS curves and the accompanying photobleaching curves. E.M and E.L. supervised the experiments. K.J., L.H-N., S.R., E.M. and E.L. wrote the paper and all co-authors assisted in refining it.

Data Availability

The following data and information is available publicly over Zenodo (https://doi.org/10.5281/zenodo.7497765): The raw fluorescence spectra, decays and anisotropy decays, the fluorescence decay fitting results, the raw in-cell fluorescence intensity trajectories, their autocorrelation curves and their analyses, the raw FLIM data and their analyses, and the full MD simulation trajectory and its analyses results.

References

1. Shu, X., Shaner, N. C., Yarbrough, C. A., Tsien, R. Y. & Remington, S. J. Novel Chromophores and Buried Charges Control Color in mFruits,. *Biochemistry* **45**, 9639–9647 (2006).
2. Arpino, J. A. J., Rizkallah, P. J. & Jones, D. D. Crystal Structure of Enhanced Green Fluorescent Protein to 1.35 Å Resolution Reveals Alternative Conformations for Glu222. *PLOS ONE* **7**, e47132–e47132 (2012).
3. Stepanenko, O. V., Stepanenko, O. V., Kuznetsova, I. M., Verkhusha, V. V. & Turoverov, K. K. Chapter Four - Beta-Barrel Scaffold of Fluorescent Proteins: Folding, Stability and Role in Chromophore Formation. in (ed. Jeon, K. W. B. T.-I. R. of C. and M. B.) vol. 302 221–278 (Academic Press, 2013).
4. Zimmerman, S. B. & Trach, S. O. Estimation of macromolecule concentrations and excluded volume effects for the cytoplasm of Escherichia coli. *Journal of Molecular Biology* **222**, 599–620 (1991).
5. Han, J. & Herzfeld, J. Macromolecular diffusion in crowded solutions. *Biophysical Journal* **65**, 1155–1161 (1993).
6. Zimmerman, S. B. & Minton, A. P. Macromolecular Crowding: Biochemical, Biophysical, and Physiological Consequences. *Annual Review of Biophysics and Biomolecular Structure* **22**, 27–65 (1993).
7. Record, M. T., Courtenay, E. S., Cayley, S. & Guttman, H. J. Biophysical compensation mechanisms buffering E. coli protein–nucleic acid interactions against changing environments. *Trends in Biochemical Sciences* **23**, 190–194 (1998).
8. Meshorer, E. *et al.* Hyperdynamic Plasticity of Chromatin Proteins in Pluripotent Embryonic Stem Cells. *Developmental Cell* **10**, 105–116 (2006).
9. Melcer, S. *et al.* Histone modifications and lamin A regulate chromatin protein dynamics in early embryonic stem cell differentiation. *Nature Communications* **3**, 910 (2012).
10. Bošković, A. *et al.* Higher chromatin mobility supports totipotency and precedes pluripotency in vivo. *Genes & development* **28**, 1042–1047 (2014).
11. Mallm, J.-P. *et al.* Glioblastoma initiating cells are sensitive to histone demethylase inhibition due to epigenetic deregulation. *International Journal of Cancer* **146**, 1281–1292 (2020).
12. Schlesinger, S. & Meshorer, E. Open Chromatin, Epigenetic Plasticity, and Nuclear Organization in Pluripotency. *Developmental Cell* **48**, 135–150 (2019).
13. Rippe, K. Liquid-Liquid Phase Separation in Chromatin. *Cold Spring Harbor perspectives in biology* (2021) doi:10.1101/cshperspect.a040683.
14. Maeshima, K., Ide, S., Hibino, K. & Sasai, M. Liquid-like behavior of chromatin. *Current Opinion in Genetics & Development* **37**, 36–45 (2016).

15. Strickfaden, H. *et al.* Condensed Chromatin Behaves like a Solid on the Mesoscale In Vitro and in Living Cells. *Cell* **183**, 1772-1784.e13 (2020).
16. Larson, A. G. *et al.* Liquid droplet formation by HP1α suggests a role for phase separation in heterochromatin. *Nature* **547**, 236–240 (2017).
17. Strom, A. R. *et al.* Phase separation drives heterochromatin domain formation. *Nature* **547**, 241–245 (2017).
18. Vakoc, C. R., Mandat, S. A., Olenchock, B. A. & Blobel, G. A. Histone H3 Lysine 9 Methylation and HP1γ Are Associated with Transcription Elongation through Mammalian Chromatin. *Molecular Cell* **19**, 381–391 (2005).
19. Zeng, W., Ball Jr, A. R. & Yokomori, K. HP1: Heterochromatin binding proteins working the genome. *Epigenetics* **5**, 287–292 (2010).
20. Meyer-Nava, S., Nieto-Caballero, V. E., Zurita, M. & Valadez-Graham, V. Insights into HP1a-Chromatin Interactions. *Cells* **9**, (2020).
21. Thierry, C. *et al.* Maintenance of Stable Heterochromatin Domains by Dynamic HP1 Binding. *Science* **299**, 721–725 (2003).
22. Festenstein, R. *et al.* Modulation of Heterochromatin Protein 1 Dynamics in Primary Mammalian Cells. *Science* **299**, 719–721 (2003).
23. Kilic, S., Bachmann, A. L., Bryan, L. C. & Fierz, B. Multivalency governs HP1α association dynamics with the silent chromatin state. *Nature Communications* **6**, 7313 (2015).
24. Kilic, S. *et al.* Single-molecule FRET reveals multiscale chromatin dynamics modulated by HP1α. *Nature Communications* **9**, 235 (2018).
25. J., V. P. *et al.* In Vivo HP1 Targeting Causes Large-Scale Chromatin Condensation and Enhanced Histone Lysine Methylation. *Molecular and Cellular Biology* **25**, 4552–4564 (2005).
26. Keenen, M. M. *et al.* HP1 proteins compact DNA into mechanically and positionally stable phase separated domains. *eLife* **10**, e64563 (2021).
27. Strom, A. R. *et al.* HP1α is a chromatin crosslinker that controls nuclear and mitotic chromosome mechanics. *eLife* **10**, e63972 (2021).
28. Ackermann, B. E. & Debelouchina, G. T. Heterochromatin Protein HP1α Gelation Dynamics Revealed by Solid-State NMR Spectroscopy. *Angewandte Chemie International Edition* **58**, 6300–6305 (2019).
29. Erdel, F. *et al.* Mouse Heterochromatin Adopts Digital Compaction States without Showing Hallmarks of HP1-Driven Liquid-Liquid Phase Separation. *Molecular Cell* **78**, 236-249.e7 (2020).
30. Muzzopappa, F. *et al.* Detecting and quantifying liquid–liquid phase separation in living cells by model-free calibrated half-bleaching. *Nature Communications* **13**, 7787 (2022).

31. Gómez-García, P. A. *et al.* Mesoscale Modeling and Single-Nucleosome Tracking Reveal Remodeling of Clutch Folding and Dynamics in Stem Cell Differentiation. *Cell Reports* **34**, (2021).
32. Novo, C. L. *et al.* Satellite repeat transcripts modulate heterochromatin condensates and safeguard chromosome stability in mouse embryonic stem cells. *Nature Communications* **13**, 3525 (2022).
33. Hyman, A. A., Weber, C. A. & Jülicher, F. Liquid-Liquid Phase Separation in Biology. *Annual Review of Cell and Developmental Biology* **30**, 39–58 (2014).
34. Alberti, S. Phase separation in biology. *Current Biology* **27**, R1097–R1102 (2017).
35. Sanchez-Burgos, I., Joseph, J. A., Collepardo-Guevara, R. & Espinosa, J. R. Size conservation emerges spontaneously in biomolecular condensates formed by scaffolds and surfactant clients. *Scientific Reports* **11**, 15241 (2021).
36. Branca, C. *et al.* Tetrahedral order in homologous disaccharide-water mixtures. *J. Chem. Phys.* **122**, 174513 (2005).
37. Chung, S. *et al.* The effect of macromolecular crowding on single-round transcription by Escherichia coli RNA polymerase. *Nucleic Acids Research* **47**, 1440–1450 (2018).
38. Wang, X. *et al.* Polyethylene Glycol Crowder's Effect on Enzyme Aggregation, Thermal Stability, and Residual Catalytic Activity. *Langmuir* **37**, 8474–8485 (2021).
39. Sung, H.-L., Sengupta, A. & Nesbitt, D. Smaller molecules crowd better: Crowder size dependence revealed by single-molecule FRET studies and depletion force modeling analysis. *J. Chem. Phys.* **154**, 155101 (2021).
40. Seefeldt, B. *et al.* Fluorescent proteins for single-molecule fluorescence applications. *Journal of Biophotonics* **1**, 74–82 (2008).
41. Štefl, M., Herbst, K., Rübsam, M., Benda, A. & Knop, M. Single-Color Fluorescence Lifetime Cross-Correlation Spectroscopy In Vivo. *Biophysical Journal* **119**, 1359–1370 (2020).
42. Pepperkok, R., Squire, A., Geley, S. & Bastiaens, P. I. H. Simultaneous detection of multiple green fluorescent proteins in live cells by fluorescence lifetime imaging microscopy. *Current Biology* **9**, 269–274 (1999).
43. Sarkisyan, K. S. *et al.* Green Fluorescent Protein with Anionic Tryptophan-Based Chromophore and Long Fluorescence Lifetime. *Biophysical Journal* **109**, 380–389 (2015).
44. Heikal, A. A., Hess, S. T., Baird, G. S., Tsien, R. Y. & Webb, W. W. Molecular spectroscopy and dynamics of intrinsically fluorescent proteins: Coral red (dsRed) and yellow (Citrine). *Proceedings of the National Academy of Sciences* **97**, 11996–12001 (2000).

45. Griesbeck, O., Baird, G. S., Campbell, R. E., Zacharias, D. A. & Tsien, R. Y. Reducing the Environmental Sensitivity of Yellow Fluorescent Protein: Mechanism and Applications. *Journal of Biological Chemistry* **276**, 29188–29194 (2001).
46. Rizzo, M. A., Springer, G. H., Granada, B. & Piston, D. W. An improved cyan fluorescent protein variant useful for FRET. *Nature Biotechnology* **22**, 445–449 (2004).
47. Wiens, M. D., Hoffmann, F., Chen, Y. & Campbell, R. E. Enhancing fluorescent protein photostability through robot-assisted photobleaching. *Integrative Biology* **10**, 419–428 (2018).
48. Kolská, Z., Valha, P., Slepička, P. & Švorčík, V. Refractometric study of systems water-poly(ethylene glycol) for preparation and characterization of Au nanoparticles dispersion. *Arabian Journal of Chemistry* **12**, 5019–5027 (2019).
49. van Manen, H.-J. *et al.* Refractive Index Sensing of Green Fluorescent Proteins in Living Cells Using Fluorescence Lifetime Imaging Microscopy. *Biophysical Journal* **94**, L67–L69 (2008).
50. Söhnel, A.-C. *et al.* Probing of protein localization and shuttling in mitochondrial microcompartments by FLIM with sub-diffraction resolution. *Biochimica et Biophysica Acta (BBA) - Bioenergetics* **1857**, 1290–1299 (2016).
51. Grange, B. W., Stevenson, W. H. & Viskanta, R. Refractive index of liquid solutions at low temperatures: an accurate measurement. *Appl. Opt.* **15**, 858–859 (1976).
52. Lakowicz, J. R. Fluorescence Anisotropy. in *Principles of Fluorescence Spectroscopy* (ed. Lakowicz, J. R.) 291–319 (Springer US, 1999). doi:10.1007/978-1-4757-3061-6_10.
53. Yang, L. *et al.* Role of Hydrogen Bonding in Green Fluorescent Protein-like Chromophore Emission. *Scientific Reports* **9**, 11640 (2019).
54. Regmi, C. K., Bhandari, Y. R., Gerstman, B. S. & Chapagain, P. P. Exploring the Diffusion of Molecular Oxygen in the Red Fluorescent Protein mCherry Using Explicit Oxygen Molecular Dynamics Simulations. *J. Phys. Chem. B* **117**, 2247–2253 (2013).
55. Sakuta, H. *et al.* Aqueous/Aqueous Micro Phase Separation: Construction of an Artificial Model of Cellular Assembly . *Frontiers in Chemistry* vol. 7 44 Preprint at (2019).
56. Annunziata, O. *et al.* Effect of polyethylene glycol on the liquid–liquid phase transition in aqueous protein solutions. *Proceedings of the National Academy of Sciences* **99**, 14165 LP – 14170 (2002).
57. Park, S. *et al.* Dehydration entropy drives liquid-liquid phase separation by molecular crowding. *Communications Chemistry* **3**, 83 (2020).
58. Lim, P. S. L. & Meshorer, E. Organization of the Pluripotent Genome. *Cold Spring Harbor perspectives in biology* **13**, (2021).

59. Farr, S. E., Woods, E. J., Joseph, J. A., Garaizar, A. & Collepardo-Guevara, R. Nucleosome plasticity is a critical element of chromatin liquid–liquid phase separation and multivalent nucleosome interactions. *Nature Communications* **12**, 2883 (2021).
60. Mattout, A. *et al.* Heterochromatin Protein 1β (HP1β) has distinct functions and distinct nuclear distribution in pluripotent versus differentiated cells. *Genome Biology* **16**, 213 (2015).
61. Harikumar, A. *et al.* An Endogenously Tagged Fluorescent Fusion Protein Library in Mouse Embryonic Stem Cells. *Stem Cell Reports* **9**, 1304–1314 (2017).
62. Maison, C. & Almouzni, G. HP1 and the dynamics of heterochromatin maintenance. *Nature Reviews Molecular Cell Biology* **5**, 296–305 (2004).
63. Aoto, T., Saitoh, N., Ichimura, T., Niwa, H. & Nakao, M. Nuclear and chromatin reorganization in the MHC-Oct3/4 locus at developmental phases of embryonic stem cell differentiation. *Developmental Biology* **298**, 354–367 (2006).
64. Bacia, K. & Schwille, P. A dynamic view of cellular processes by in vivo fluorescence auto- and cross-correlation spectroscopy. *Methods* **29**, 74–85 (2003).
65. Kim, S. A., Heinze, K. G. & Schwille, P. Fluorescence correlation spectroscopy in living cells. *Nature Methods* **4**, 963–973 (2007).
66. Taylor, N. O., Wei, M.-T., Stone, H. A. & Brangwynne, C. P. Quantifying Dynamics in Phase-Separated Condensates Using Fluorescence Recovery after Photobleaching. *Biophysical Journal* **117**, 1285–1300 (2019).
67. Boersma, A. J., Zuhorn, I. S. & Poolman, B. A sensor for quantification of macromolecular crowding in living cells. *Nature Methods* **12**, 227–229 (2015).
68. Liu, B. *et al.* Design and Properties of Genetically Encoded Probes for Sensing Macromolecular Crowding. *Biophysical Journal* **112**, 1929–1939 (2017).
69. Stepanenko, O. V. *et al.* Comparative Studies on the Structure and Stability of Fluorescent Proteins EGFP, zFP506, mRFP1, “dimer2”, and DsRed1. *Biochemistry* **43**, 14913–14923 (2004).
70. Campbell, B. C., Paez-Segala, M. G., Looger, L. L., Petsko, G. A. & Liu, C. F. Chemically stable fluorescent proteins for advanced microscopy. *Nature Methods* **19**, 1612–1621 (2022).
71. Voliani, V. *et al.* Cis−Trans Photoisomerization of Fluorescent-Protein Chromophores. *J. Phys. Chem. B* **112**, 10714–10722 (2008).
72. Rafiq, S., Rajbongshi, B. K., Nair, N. N., Sen, P. & Ramanathan, G. Excited State Relaxation Dynamics of Model Green Fluorescent Protein Chromophore Analogs: Evidence for Cis–Trans Isomerism. *J. Phys. Chem. A* **115**, 13733–13742 (2011).
73. Mooney, C. R. S. *et al.* Taking the green fluorescence out of the protein: dynamics of the isolated GFP chromophore anion. *Chem. Sci.* **4**, 921–927 (2013).

74. Conyard, J. *et al.* A new twist in the photophysics of the GFP chromophore: a volume-conserving molecular torsion couple. *Chem. Sci.* **9**, 1803–1812 (2018).
75. Jones, C. M., List, N. H. & Martínez, T. J. Resolving the ultrafast dynamics of the anionic green fluorescent protein chromophore in water. *Chem. Sci.* **12**, 11347–11363 (2021).
76. Chatterjee, S., Ahire, K. & Karuso, P. Room-Temperature Dual Fluorescence of a Locked Green Fluorescent Protein Chromophore Analogue. *J. Am. Chem. Soc.* **142**, 738–749 (2020).
77. Nienhaus, K., Nar, H., Heilker, R., Wiedenmann, J. & Nienhaus, G. U. Trans−Cis Isomerization is Responsible for the Red-Shifted Fluorescence in Variants of the Red Fluorescent Protein eqFP611. *J. Am. Chem. Soc.* **130**, 12578–12579 (2008).
78. Romei, M. G., Lin, C.-Y., Mathews, I. I. & Boxer, S. G. Electrostatic control of photoisomerization pathways in proteins. *Science* **367**, 76–79 (2020).
79. Allen, J. R., Ross, S. T. & Davidson, M. W. Single molecule localization microscopy for superresolution. *Journal of Optics* **15**, 094001 (2013).
80. Lelek, M. *et al.* Single-molecule localization microscopy. *Nature Reviews Methods Primers* **1**, 39–39 (2021).
81. Hendrix, J., Flors, C., Dedecker, P., Hofkens, J. & Engelborghs, Y. Dark States in Monomeric Red Fluorescent Proteins Studied by Fluorescence Correlation and Single Molecule Spectroscopy. *Biophysical Journal* **94**, 4103–4113 (2008).
82. Stoddard, A. & Rolland, V. I see the light! Fluorescent proteins suitable for cell wall/apoplast targeting in Nicotiana benthamiana leaves. *Plant Direct* **3**, e00112 (2019).
83. Bhattacharya, D., Talwar, S., Mazumder, A. & Shivashankar, G. V. Spatio-Temporal Plasticity in Chromatin Organization in Mouse Cell Differentiation and during Drosophila Embryogenesis. *Biophysical Journal* **96**, 3832–3839 (2009).
84. Morozumi, Y. *et al.* Atad2 is a generalist facilitator of chromatin dynamics in embryonic stem cells. *Journal of Molecular Cell Biology* **8**, 349–362 (2016).
85. Christogianni, A. *et al.* Heterochromatin remodeling in embryonic stem cells proceeds through stochastic de-stabilization of regional steady-states. *Biochimica et Biophysica Acta (BBA) - Gene Regulatory Mechanisms* **1860**, 661–673 (2017).
86. Efroni, S. *et al.* Global Transcription in Pluripotent Embryonic Stem Cells. *Cell Stem Cell* **2**, 437–447 (2008).
87. Campbell, R. E. *et al.* A monomeric red fluorescent protein. *Proceedings of the National Academy of Sciences* **99**, 7877 LP – 7882 (2002).
88. Hülya Kuduğ , Bahadır Ataman , Rizvan İmamoğlu , Duygu Düzgün, İ. G. Production of red fluorescent protein (mCherry) in an inducible E. coli expression system in a bioreactor, purification and characterization. *International Advanced Researches and Engineering Journal* **3**, 20–25 (219AD).

89. Beechem, J. M. & Haas, E. Simultaneous Determination of Intramolecular Distance Distributions and Conformational Dynamics by Global Analysis of Energy Transfer Measurements. *Biophysical Journal* **55**, 1225–1236 (1989).
90. Huang, F. *et al.* Time-resolved fluorescence resonance energy transfer study shows a compact denatured state of the B domain of protein A. *Biochemistry* **48**, 3468–3476 (2009).
91. Song, L., Hennink, E. J., Young, I. T. & Tanke, H. J. Photobleaching kinetics of fluorescein in quantitative fluorescence microscopy. *Biophysical Journal* **68**, 2588–2600 (1995).
92. Marcu, L., Grundfest, W. S. & Maarek, J.-M. I. Photobleaching of Arterial Fluorescent Compounds: Characterization of Elastin, Collagen and Cholesterol Time-resolved Spectra during Prolonged Ultraviolet Irradiation. *Photochemistry and Photobiology* **69**, 713–721 (1999).
93. Jo, S., Kim, T., Iyer, V. G. & Im, W. CHARMM-GUI: A web-based graphical user interface for CHARMM. *Journal of Computational Chemistry* **29**, 1859–1865 (2008).
94. Pettersen, E. F. *et al.* UCSF Chimera—A visualization system for exploratory research and analysis. *Journal of Computational Chemistry* **25**, 1605–1612 (2004).
95. Fiser, A., Do, R. K. G. & Šali, A. Modeling of loops in protein structures. *Protein Science* **9**, 1753–1773 (2000).
96. Shen, M. & Sali, A. Statistical potential for assessment and prediction of protein structures. *Protein Science* **15**, 2507–2524 (2006).
97. Berendsen, H. J. C., van der Spoel, D. & van Drunen, R. GROMACS: A message-passing parallel molecular dynamics implementation. *Computer Physics Communications* **91**, 43–56 (1995).
98. Abraham, M. J. *et al.* GROMACS: High performance molecular simulations through multi-level parallelism from laptops to supercomputers. *SoftwareX* **1–2**, 19–25 (2015).
99. Regmi, Chola K. Structural Flexibility and Oxygen Diffusion Pathways in Monomeric Fluorescent Proteins. (FIU, 2014).
100. Huang, J. *et al.* CHARMM36m: an improved force field for folded and intrinsically disordered proteins. *Nature Methods* **14**, 71–73 (2017).
101. MacKerell, A. D. Jr. *et al.* All-Atom Empirical Potential for Molecular Modeling and Dynamics Studies of Proteins. *J. Phys. Chem. B* **102**, 3586–3616 (1998).
102. Bussi, G., Donadio, D. & Parrinello, M. Canonical sampling through velocity rescaling. *J. Chem. Phys.* **126**, 014101 (2007).
103. Berendsen, H. J. C., Postma, J. P. M., van Gunsteren, W. F., DiNola, A. & Haak, J. R. Molecular dynamics with coupling to an external bath. *J. Chem. Phys.* **81**, 3684–3690 (1984).
104. Parrinello, M. & Rahman, A. Polymorphic transitions in single crystals: A new molecular dynamics method. *Journal of Applied Physics* **52**, 7182–7190 (1981).

105. Hess, B., Bekker, H., Berendsen, H. J. C. & Fraaije, J. G. E. M. LINCS: A linear constraint solver for molecular simulations. *Journal of Computational Chemistry* **18**, 1463–1472 (1997).

106. Miyamoto, S. & Kollman, P. A. Settle: An analytical version of the SHAKE and RATTLE algorithm for rigid water models. *Journal of Computational Chemistry* **13**, 952–962 (1992).

107. Darden, T., York, D. & Pedersen, L. Particle mesh Ewald: An N·log(N) method for Ewald sums in large systems. *J. Chem. Phys.* **98**, 10089–10092 (1993).

108. Hoover, W. G. Canonical dynamics: Equilibrium phase-space distributions. *Phys. Rev. A* **31**, 1695–1697 (1985).

109. Michaud-Agrawal, N., Denning, E. J., Woolf, T. B. & Beckstein, O. MDAnalysis: A toolkit for the analysis of molecular dynamics simulations. *Journal of Computational Chemistry* **32**, 2319–2327 (2011).

110. Zhou, Qian-Yi, Park, Jaesik, & Koltun, Vladlen. Open3D: A modern library for 3D data processing. Preprint at https://doi.org/10.48550/arXiv.1801.09847 (2018).

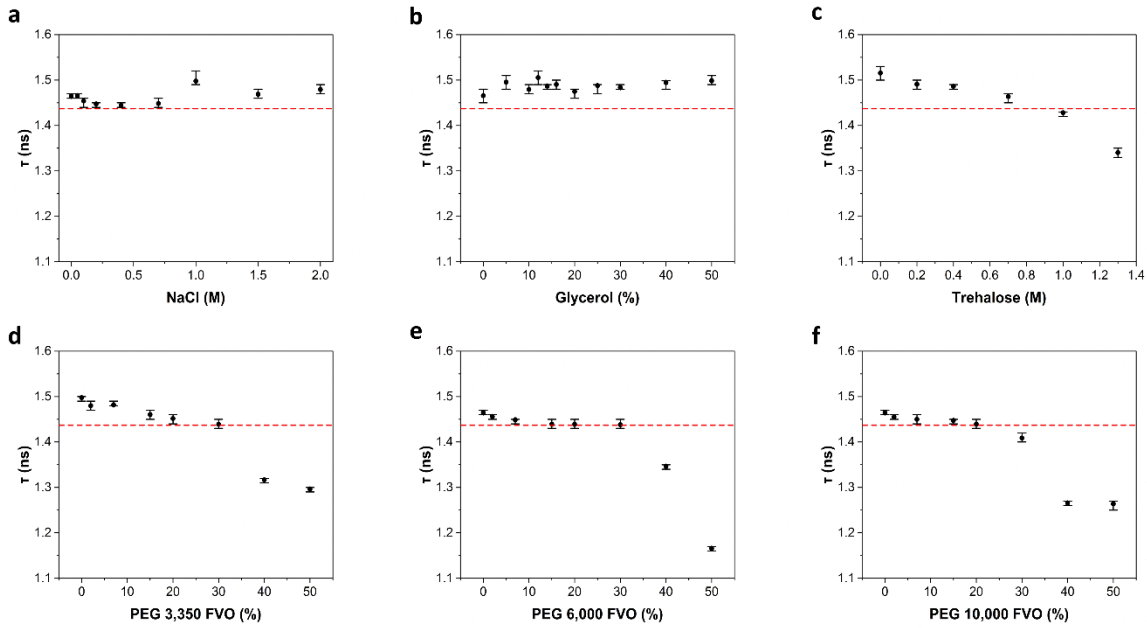

Fig. 1 | The mean fluorescence lifetime of mCherry at different physico-chemical conditions. a-f, mean fluorescence lifetime (τ) of 100 nM mCherry as a measure of increasing NaCl concentrations **a**, Glycerol, **b**, Trehalose, **c**, and **d-f**, PEG. Crowding exclusively induces lifetime reduction, and only above 30% FVO. The values and error estimates are based on calculations (Supplementary equation (2)) using best-fit values of the recorded fluorescence decays (Fig. S1) to a sum of two exponents function (Supplementary equation (1)). The values of the intrinsic mean fluorescence lifetimes are reported in Table S1. The error estimates are the minimal and maximal intrinsic mean fluorescence lifetime values calculated from all lifetime component values and their amplitudes, which are within a reduced χ^2 that is within 95% confidence relative to the minimal best-fit reduced χ^2 value. Red line that is set at 1.44 ns highlights the limit below which fluorescence lifetimes drop in the presence of elevated concentrations of PEG or trehalose.

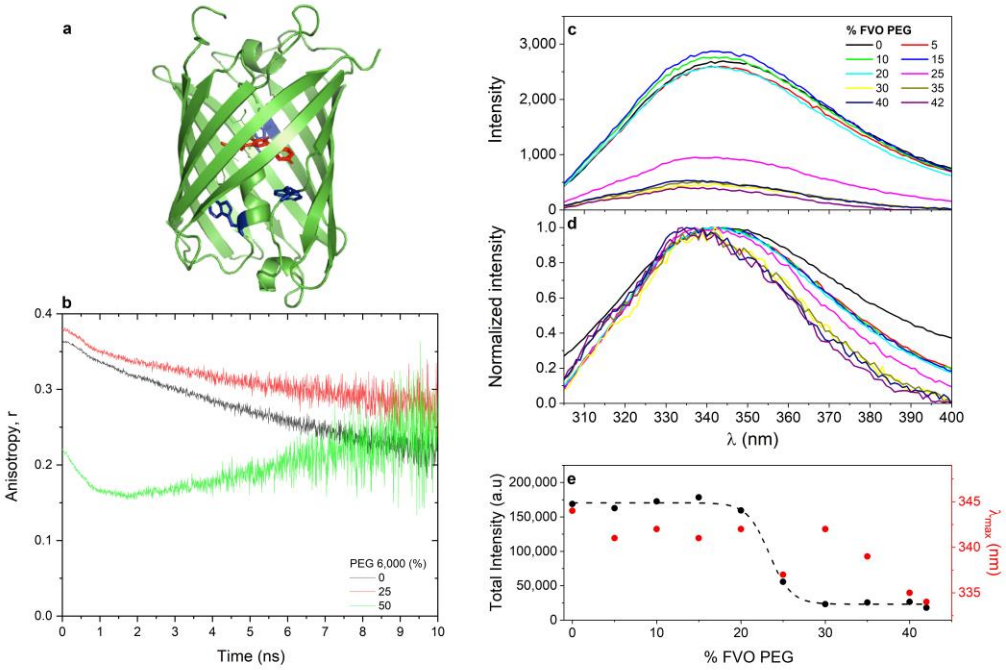

Fig. 2 | Spectroscopic characterization of increase in degrees of freedom in the interior of mCherry. a, The fluorophore group of mCherry (red) and the three Trp residues of mCherry (blue) pointing towards the interior of mCherry (green). **b,** Time-resolved fluorescence anisotropy of 100 nM mCherry show inner degrees of freedom of fluorophore increase. Shown are the fluorescence anisotropy decays of mCherry in the absence of PEG 6,000 (black) and in the presence of 25% (red) and 50% (green) FVO of PEG 6,000, where only above 30% FVO a rapidly decaying component shows up, on top of the overall slowdown due to increase in viscosity and decrease in fluorescence lifetime. **c-e,** Trp fluorescence spectra report on increase in FP interior degrees of freedom. The fluorescence spectra of the three Trp residues of 10 µM mCherry were recorded as a function of increasing FVO of PEG and are reported without normalization (**c**), and after normalization (**d**), and the area below the fluorescence spectra (**e**, black dots) and the wavelength at which fluorescence intensity is maximal (**e**, red dots) were reported. Note that the trend in the area below spectra was fit to a sigmoidal curve (**e**, dashed black line), with a best-fit midpoint at 23.3±0.3% FVO of PEG.

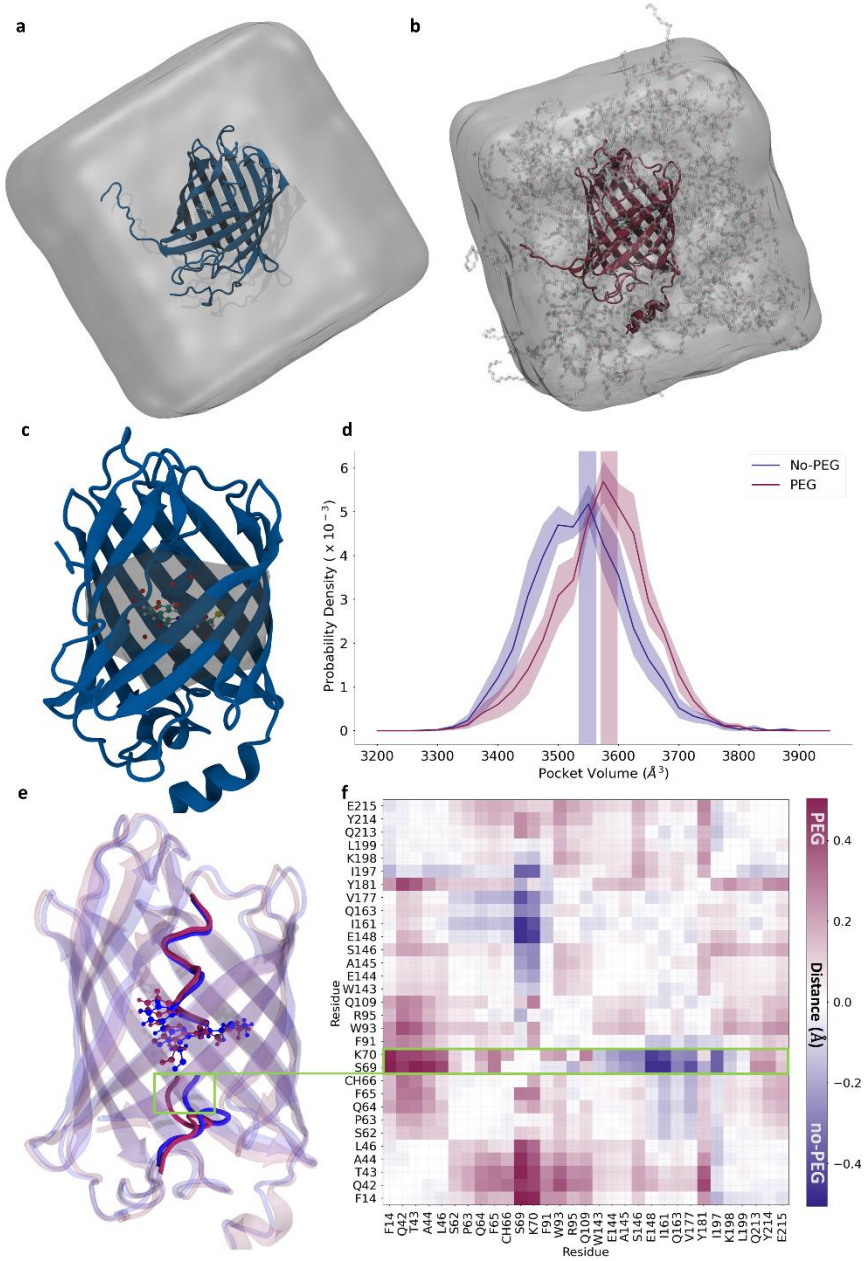

Fig. 3 | Conformational change of the fluorophore pocket in the presence of PEG. a-b, Simulated systems of mCherry in water (**a**) and mCherry in water and 42% FVO PEG (**b**). **c,** mCherry with the fluorophore pocket (formed by the 30 residues shown in Table S2) shaded in. The fluorophore is shown in a ball and stick representation and water molecules are shown as red spheres. The structure is taken from simulations. **d,** The distribution of the pocket volume for both the PEG and no-PEG systems. The PEG system is shown in plum and no-PEG is shown in navy blue. Shaded regions indicate the standard error of the mean, treating each trajectory as an independent observation. **e,** Representative 3D structures from the simulations showing helix conformations for the PEG (plum) and no-PEG (navy) systems. Residues S69 and K70 are highlighted in a green box. **f,** The difference map of average fluorophore-pocket C_α-C_α distances. Distances that are larger in the PEG system are positive and shown in plum, and distances that are larger in the no-PEG system are negative and shown in navy blue.

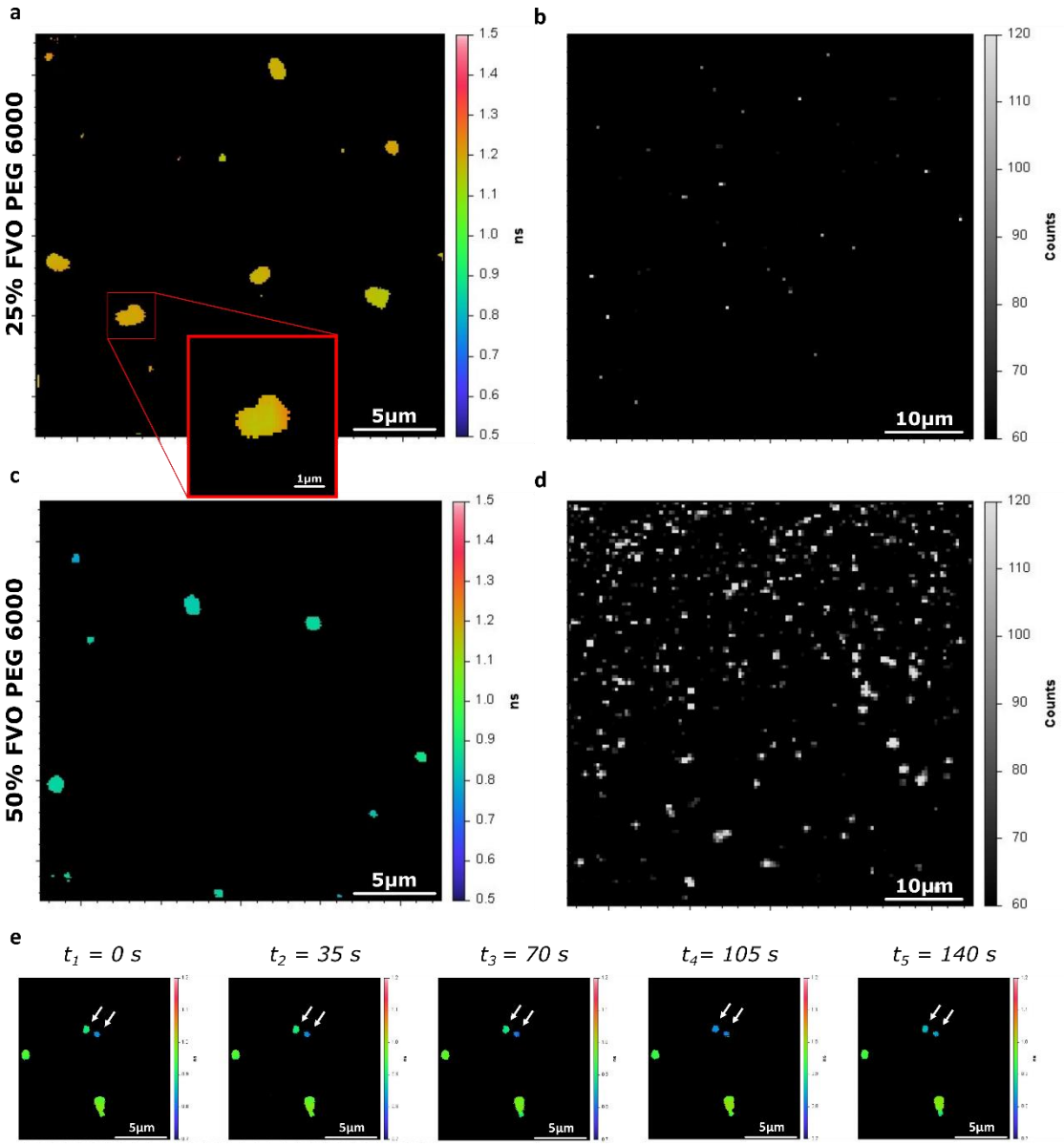

Fig. 4 | Fluorescence intensity and lifetimes of PEG-induced *in vitro* mCherry precipitates. **a-d**, Fluorescence lifetime (**a, c**) and intensity (**b, d**) images of mCherry PEG 6,000-induced *in vitro* precipitates formed after adding mCherry at a total concentration of 100 nM in a solution containing 25% FVO (**a**, **b**) and 50% FVO (**c**, **d**) PEG 6,000. **e**, A few frames from a time series of fluorescence lifetime images of mCherry precipitates formed in a solution containing 50% PEG 6,000, with white arrows pointing on precipitates with visible changes in fluorescence lifetime over the course of 140 seconds, but with a homogeneity of lifetime values in each time point for each precipitate.

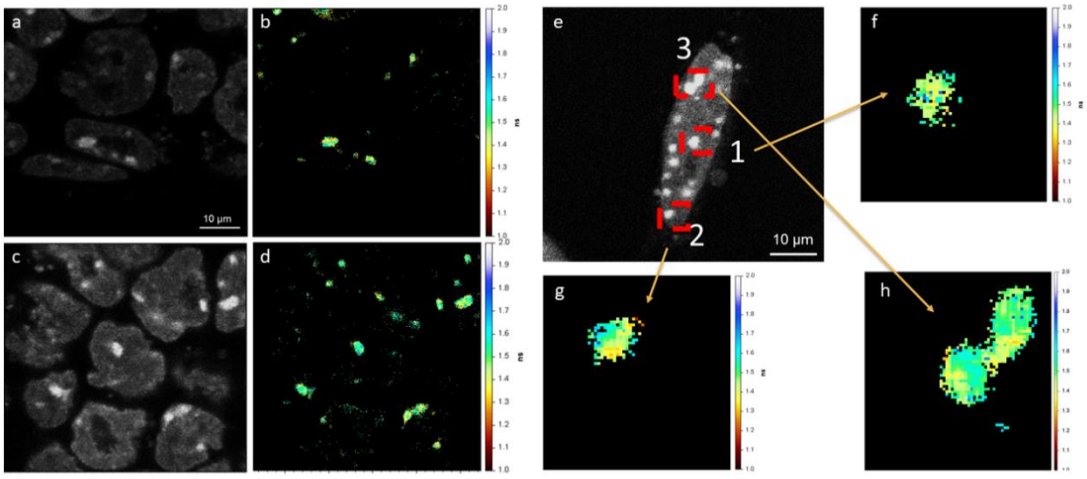

Fig. 5 | FLIM of mCherry-HP1α condensates in undifferentiated and early-differentiated ESCs report on their inner density heterogeneities. a-d, Undifferentiated ESCs. Figures report two examples of 60x60 µm^2 frames with mCherry-HP1α condensates in undifferentiated ESCs, both fluorescence intensity (**a, c**) and fluorescence lifetime (**b, d**). **e-h,** Early-differentiated ESCs. Figures reports an example 60x60 µm^2 frame with mCherry-HP1α condensates in early-differentiated ESCs fluorescence intensity (**e**) image, and then the fluorescence lifetime images of three foci in other panels (**f-h**). Scale bar in panel **a** represent the same scales as in panels **b-d**.

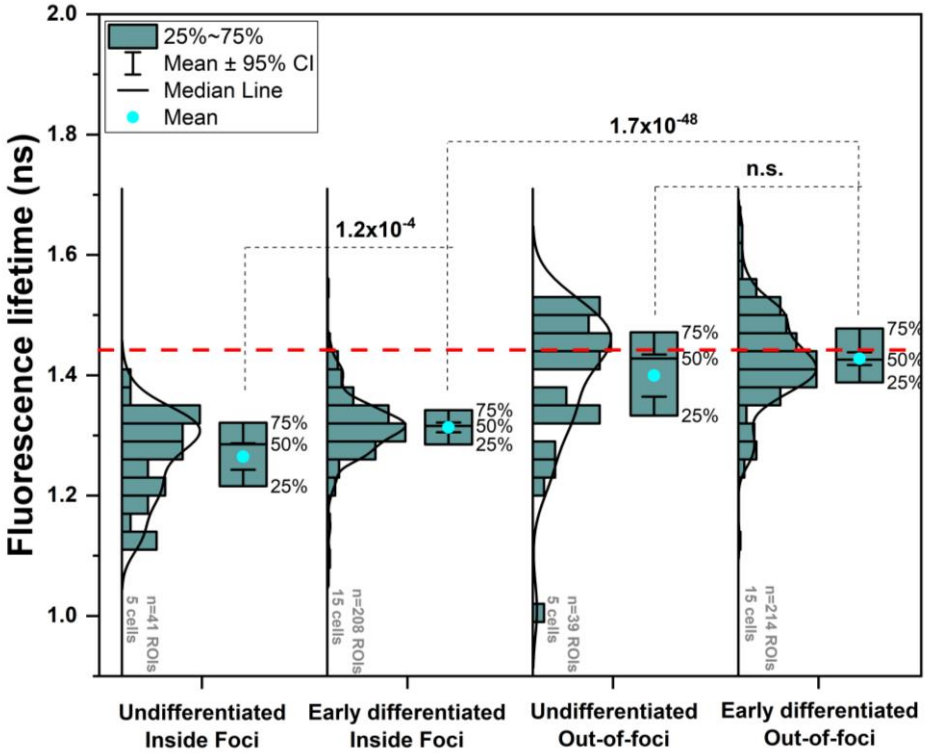

Fig. 6 | Summary of mean fluorescence lifetimes inside and out of mCherry-HP1α foci for multiple imaged cells. Mean fluorescence lifetimes acquired from multiple region of interests (ROIs) inside and out of mCherry-HP1α foci from multiple cells in undifferentiated and early differentiated ESCs, and how they distribute compared to mean and median fluorescence lifetimes. The histograms of mean fluorescence lifetimes are shown as vertical bar plots, and kernel density is added on top of them (smooth black curves). The figure reports the fluorescence lifetimes statistics in a box plot including the mean, median, 25-75% percentile range, 95% confidence interval and the p-values of two samples T-test between different pairs of samples. A horizontal red line shows the 1.44 ns lower boundary of mCherry fluorescence lifetime below which the crowdedness level is above 30% FVO (Fig. 1).